

Multi-wavelength study of triggered star formation around the mid-infrared bubble N14

L. K. Dewangan^{1,2★} and D. K. Ojha¹

¹Department of Astronomy and Astrophysics, Tata Institute of Fundamental Research, Homi Bhabha Road, Mumbai 400 005, India

²Centro de Astrofísica da Universidade do Porto, Rua das Estrelas, 4150-762 s/n Porto, Portugal

Accepted 2012 November 15. Received 2012 November 15; in original form 2012 August 24

ABSTRACT

We present multi-wavelength analysis around the mid-infrared (MIR) bubble N14 to probe the signature of triggered star formation as well as the formation of new massive star(s) and/or cluster(s) at the borders of the bubble by the expansion of the H II region. *Spitzer* Infrared Array Camera ratio maps reveal that the bubble is traced by the polycyclic aromatic hydrocarbon emission following an almost circular morphology except in the south-west direction towards the low molecular density environment. The observational signatures of the collected molecular and cold dust material have been found around the bubble. We have detected 418 young stellar objects (YSOs) in the selected region around the bubble N14. Interestingly, the detected YSO clusters are associated with the collected molecular and cold dust material at the borders of the bubble. One of the clusters is found with deeply embedded intermediate mass and massive Class I YSOs associated with one of the dense dust clumps in the east of the bubble N14. We do not find good agreement between the dynamical age of the H II region and the fragmentation time of the accumulated molecular materials to explain the possible ‘collect-and-collapse’ process around the bubble N14. Therefore, we suggest the possibility of triggered star formation by compression of the pre-existing dense clumps by the shock wave and/or small-scale Jeans gravitational instabilities in the collected materials. We have also investigated 5 young massive embedded protostars (8–10 M_⊙) and 15 intermediate mass (3–7 M_⊙) Class I YSOs which are associated with the dust and molecular fragmented clumps at the borders of the bubble. We conclude that the expansion of the H II region is also leading to the formation of these intermediate and massive Class I YSOs around the bubble N14.

Key words: stars: formation – stars: pre-main-sequence – ISM: bubbles – dust, extinction – H II regions – ISM: individual objects (IRAS 18134–1652).

1 INTRODUCTION

Massive stars ($M > 8 M_{\odot}$) have the ability to interact with the surrounding cloud with their energetic wind, UV ionizing radiation and an expanding H II region (Zinnecker & Yorke 2007). In recent years, mid-infrared (MIR) shells or bubbles around the expanding H II regions have been recognized as the sites to observationally investigate the conditions of sequential/triggered star formation (Elmegreen & Lada 1977; Elmegreen 2010, and references therein) and the formation of new massive star(s) and/or cluster(s) as well. Two mechanisms have been proposed to explain the observed star formation due to the influence of massive star(s): ‘collect

and collapse’ (Elmegreen & Lada 1977; Whitworth et al. 1994) and radiation-driven implosion (RDI; Bertoldi 1989; Lefloch & Lazareff 1994). In the ‘collect and collapse’ scenario, the H II region expands and accumulates molecular material between the ionization and the shock fronts. With time the collected material becomes unstable and fragments into several clumps, which leads to the formation of new generation of stars, as an effect of the shocks. In the RDI model, the expanding H II region supplies enough external pressure to initiate collapse of a pre-existing dense clump in the molecular material.

In this work, we present a multi-wavelength study of an MIR bubble N14 associated with IRAS 18134–1652, from the catalogue of Churchwell et al. (2006, 2007) around the Galactic H II region G014.0–00.1. The bubble N14 is situated at a near distance of 3.5 kpc (Beaumont & Williams 2010) and is associated with the water maser near (~ 33 arcsec) to the IRAS position (Codella

★E-mail: Lokesh.Dewangan@astro.up.pt

et al. 1994). Lockman (1989) reported the velocity of ionized gas (v_{LSR}) to be about 36 km s^{-1} near to the IRAS position, using a hydrogen recombination line study. Beaumont & Williams (2010) and Deharveng et al. (2010) studied several MIR bubbles including N14 using the James Clerk Maxwell Telescope (JCMT) $^{12}\text{CO}(J = 3-2)$ line and the APEX Telescope Large Area Survey of the Galactic plane at $870 \mu\text{m}$ (ATLASGAL) continuum observations, respectively. Beaumont & Williams (2010) also reported 20 cm Multi-Array Galactic Plane Imaging Survey (MAGPIS) radio continuum data around N14. They estimated molecular gas velocity to be about 40.3 km s^{-1} associated with the bubble N14 with the velocity dispersion of 2.8 km s^{-1} . They also listed about six O9.5 stars to produce the observed MAGPIS 20 cm integrated flux ($\sim 2.41 \text{ Jy}$) for the H II region associated with the bubble N14. Deharveng et al. (2010) found three dense clumps around the bubble N14 and stated that the bubble is broken in the direction of the low density region.

Previous studies on this region therefore clearly reveal the presence of molecular, cold dust as well as ionized emissions in the bubble. In this paper, we present multi-wavelength observations to study the interaction of the H II region with the surrounding interstellar medium (ISM). Our study will allow us to investigate the star formation especially the identification of embedded populations and also explore whether there is any evidence to form stars by the triggering effect of the H II region around the bubble N14.

In Section 2, we introduce the archival data and data reduction procedures used for the present study. In Section 3, we examine the structure of the MIR bubble N14 at different wavelengths and the interaction of massive stars with their environment using various *Spitzer* MIR ratio maps. In this section, we also describe the selection of young populations, their distribution around the bubble and identification of ionizing candidates, and discuss the triggered star formation scenario at the borders of the bubble. In Section 4, we summarize our conclusions.

2 AVAILABLE DATA AND DATA REDUCTION

Archival deep near-infrared (NIR) HK_s images and a catalogue around the bubble N14 were obtained from the UKIDSS 6th archival data release (UKIDSSDR6plus) of the Galactic Plane Survey (GPS; Lawrence et al. 2007). It is to be noted that there is no GPS J -band observation available for the bubble N14. UKIDSS observations were made using the UKIRT Wide Field Camera (WFCAM; Casali et al. 2007) and fluxes were calibrated using Two Micron All Sky Survey (2MASS; Skrutskie et al. 2006). The details of basic data reduction and calibration procedures are described in Dye et al. (2006) and Hodgkin et al. (2009), respectively. Magnitudes of bright stars ($H \leq 11.5 \text{ mag}$ and $K_s \leq 10.5 \text{ mag}$) were obtained from the 2MASS, due to saturation of UKIDSS bright sources. Only those sources are selected for the study which have the photometric magnitude error of 0.1 and less in each band to ensure good photometric quality.

We obtained narrow-band molecular hydrogen (H_2 ; $2.12 \mu\text{m}$; $1-0 \text{ S}(1)$) imaging data from the UWISH2 survey (Froebrich et al. 2011). We followed a procedure similar to that described by Varricatt (2011) to obtain the final continuum-subtracted H_2 image using the GPS K_s image.

The *Spitzer* Space Telescope Infrared Array Camera [IRAC; Ch1 ($3.6 \mu\text{m}$), Ch2 ($4.5 \mu\text{m}$), Ch3 ($5.8 \mu\text{m}$) and Ch4 ($8.0 \mu\text{m}$); Fazio et al. 2004 and Multiband Imaging Photometer [MIPS ($24 \mu\text{m}$); Rieke et al. 2004 archival images were obtained around the N14 region from the ‘Galactic Legacy Infrared Mid-Plane Survey Extraordinaire’ (GLIMPSE; Benjamin et al. 2003; Churchwell et al.

2009) and ‘A 24 and 70 Micron Survey of the Inner Galactic Disk with MIPS’ (MIPSGAL; Carey et al. 2005) surveys. The MIPSGAL $24 \mu\text{m}$ image is saturated close to the IRAS position inside the bubble N14. We used the GLIMPSE-I Spring ‘07 highly reliable Point-Source Catalog and also performed aperture photometry on all the GLIMPSE images (plate scale of 0.6 arcsec/pixel) using a 2.4 arcsec aperture and a sky annulus from 2.4 to 7.3 arcsec using IRAF^1 for those sources detected in images, but the photometric magnitudes are not available in the GLIMPSE-I catalogue. The IRAC/GLIMPSE photometry is calibrated using zero magnitudes including aperture corrections, 18.5931 (Ch1), 18.0895 (Ch2), 17.4899 (Ch3) and 16.6997 (Ch4), obtained from *IRAC Instrument Handbook* (Version 1.0, 2010 February).

We obtained a 20 cm radio continuum map (resolution $\sim 6 \text{ arcsec}$) from the Very Large Array MAGPIS (Helfand et al. 2006) to trace the ionized region around N14. The molecular $^{12}\text{CO}(J = 3-2)$ (rest frequency 345.7959899 GHz) spectral line public processed archival data were also utilized in the present work. The CO observations (project id: M10BD02) were taken on 2010 August 22 at the 15 m JCMT using the HARP array. An archival BOLOCAM 1.1 mm (Aguirre et al. 2011) image (with the effective FWHM Gaussian beam size of $\sim 33 \text{ arcsec}$) was also used in the present work.

3 RESULTS AND DISCUSSION

3.1 Multi-wavelength view of the bubble N14

Fig. 1 shows the selected region ($\sim 12 \times 8.6 \text{ arcmin}^2$) around the bubble N14, made of the three-colour composite image using GLIMPSE [$8.0 \mu\text{m}$ (red) and $4.5 \mu\text{m}$ (green)] and UKIDSS K_s (blue). The $8 \mu\text{m}$ band contains the two strongest polycyclic aromatic hydrocarbon (PAH) features at 7.7 and $8.6 \mu\text{m}$, which are excited in the photodissociation region (or the photon-dominated region, or PDR). The PDRs are the interface between neutral and molecular hydrogen and traced by PAH emissions. PAH emission is also known to be the tracer of ionization fronts. The positions of IRAS 18134–1652 (+) and water maser (\times) (Codella et al. 1994) are marked in the figure. Fig. 1 displays an almost circular morphology of the MIR bubble N14 prominently around IRAS 18134–1652. These bubble structures are not seen in any of the UKIDSS NIR images, but prominently visible in all GLIMPSE images. JCMT molecular gas (JCMT CO 3–2) emission contours are also overlaid in Fig. 1 with 20, 40, 60, 80 and 95 per cent of the peak value, i.e. $60.43 \text{ K km s}^{-1}$. The peak positions of the three detected $870 \mu\text{m}$ dense clumps (Deharveng et al. 2010) are also marked by a big star symbol in the figure. Fig. 2 shows a colour composite image made using the MIPSGAL $24 \mu\text{m}$ (red), GLIMPSE $8 \mu\text{m}$ (green) and $3.6 \mu\text{m}$ (blue) images, overlaid by the BOLOCAM 1.1 mm emission by solid yellow contours. The MIPS $24 \mu\text{m}$ image is saturated near to the IRAS position, but a few point sources are also seen around the bubble. The MAGPIS 20 cm radio continuum emission is also overlaid in Fig. 2 by black contours. The cold dust emission at 1.1 mm is very dense and prominent at the borders of the bubble. It is clearly seen that the peaks of $870 \mu\text{m}$, 1.1 mm dust emission and CO molecular gas emissions are spatially coincident along the borders of the bubble (see Figs 1 and 2). The $24 \mu\text{m}$ and 20 cm images trace the warm dust and ionized gas in the region, respectively. It is obvious from Fig. 2 that the PDR (traced by $8 \mu\text{m}$)

¹IRAF is distributed by the National Optical Astronomy Observatory, USA.

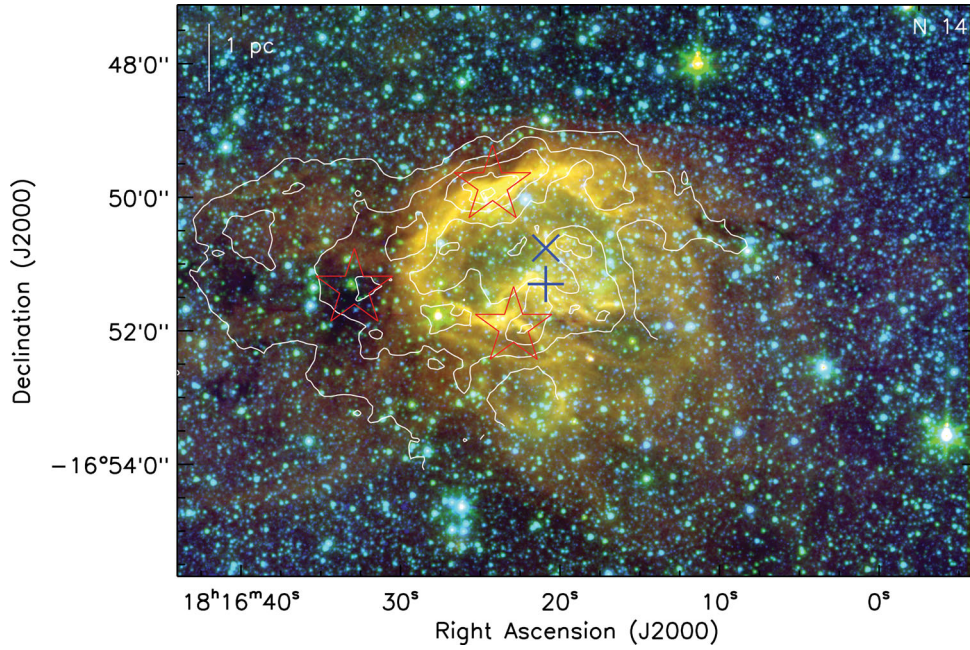


Figure 1. Three-colour composite image (size $\sim 12 \times 8.6$ arcmin 2 ; central coordinates: $\alpha_{2000} = 18^{\text{h}} 16^{\text{m}} 18^{\text{s}}.9$, $\delta_{2000} = -16^{\circ} 51' 25''.2$) of the selected region around the bubble N14, using *Spitzer*-GLIMPSE images at $8.0 \mu\text{m}$ (red), $4.5 \mu\text{m}$ (green) and UKIDSS K_s (blue) in the log scale. Archival JCMT molecular ^{12}CO (3–2) gas emission contours are also overlaid on the image with 20, 40, 60, 80 and 95 per cent of the peak value, i.e. $60.43 \text{ K km s}^{-1}$. The positions of the three $870 \mu\text{m}$ dust clumps from Deharveng et al. (2010) are marked by big red star symbols in the image. The scale bar on the top-left shows a size of 1 pc at the distance of 3.5 kpc. The positions of IRAS 18134–1652 (+) and water maser (x) are marked in the figure.

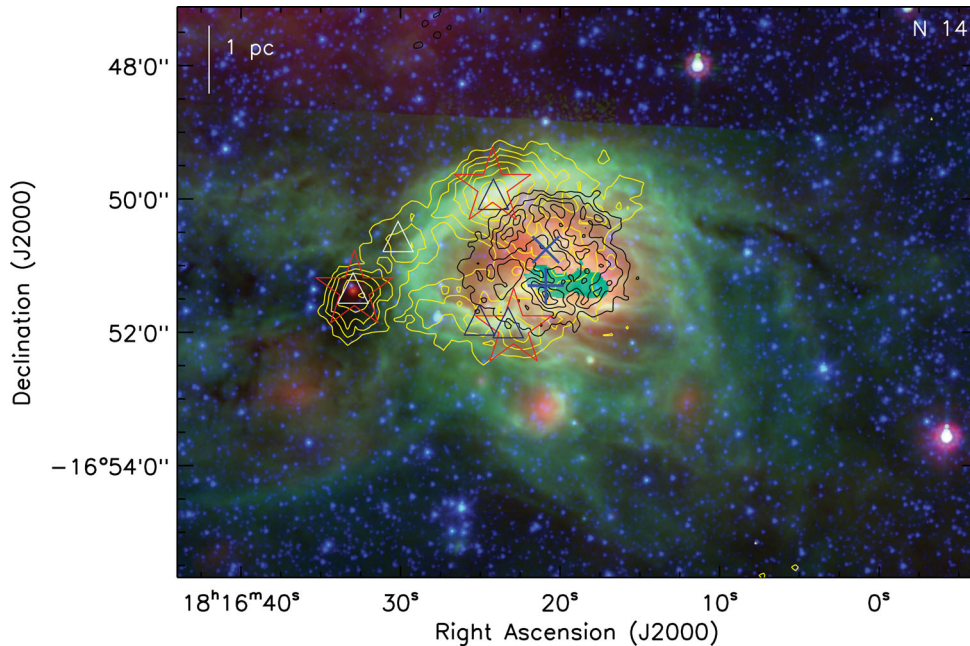


Figure 2. 20 cm contours in black colour around the bubble N14 obtained from the MAGPIS survey, overlaid on a colour composite image made using the $24 \mu\text{m}$ (red), $8 \mu\text{m}$ (green) and $3.6 \mu\text{m}$ (blue) images. The 20 cm contour levels are 40, 55, 70, 85 and 95 per cent of the peak value, i.e. $0.0115 \text{ Jy beam}^{-1}$. The BOLOCAM 1.1 mm emission is also shown by solid yellow contours with 20, 30, 40, 55, 70, 85 and 95 per cent of the peak value, i.e. $1.07 \text{ Jy beam}^{-1}$. The peak positions of BOLOCAM 1.1 mm clumps are shown by triangle symbols obtained from the Bolocam Galactic Plane Survey (BGPS) catalogue. The other marked symbols are similar to those shown in Fig. 1 (see the text for more details). The MIPS $24 \mu\text{m}$ image is saturated near the IRAS position.

encloses $24 \mu\text{m}$ dust and 20 cm ionized emissions inside the bubble and indicates the presence of dust and gas in and around the H II region (see e.g. Watson et al. 2008, for the N10, N21 and N49 bubbles).

3.2 PAH emission and the collected material

In recent years, *Spitzer*-IRAC bands and ratio maps have been utilized to study the interaction of massive stars with their immediate

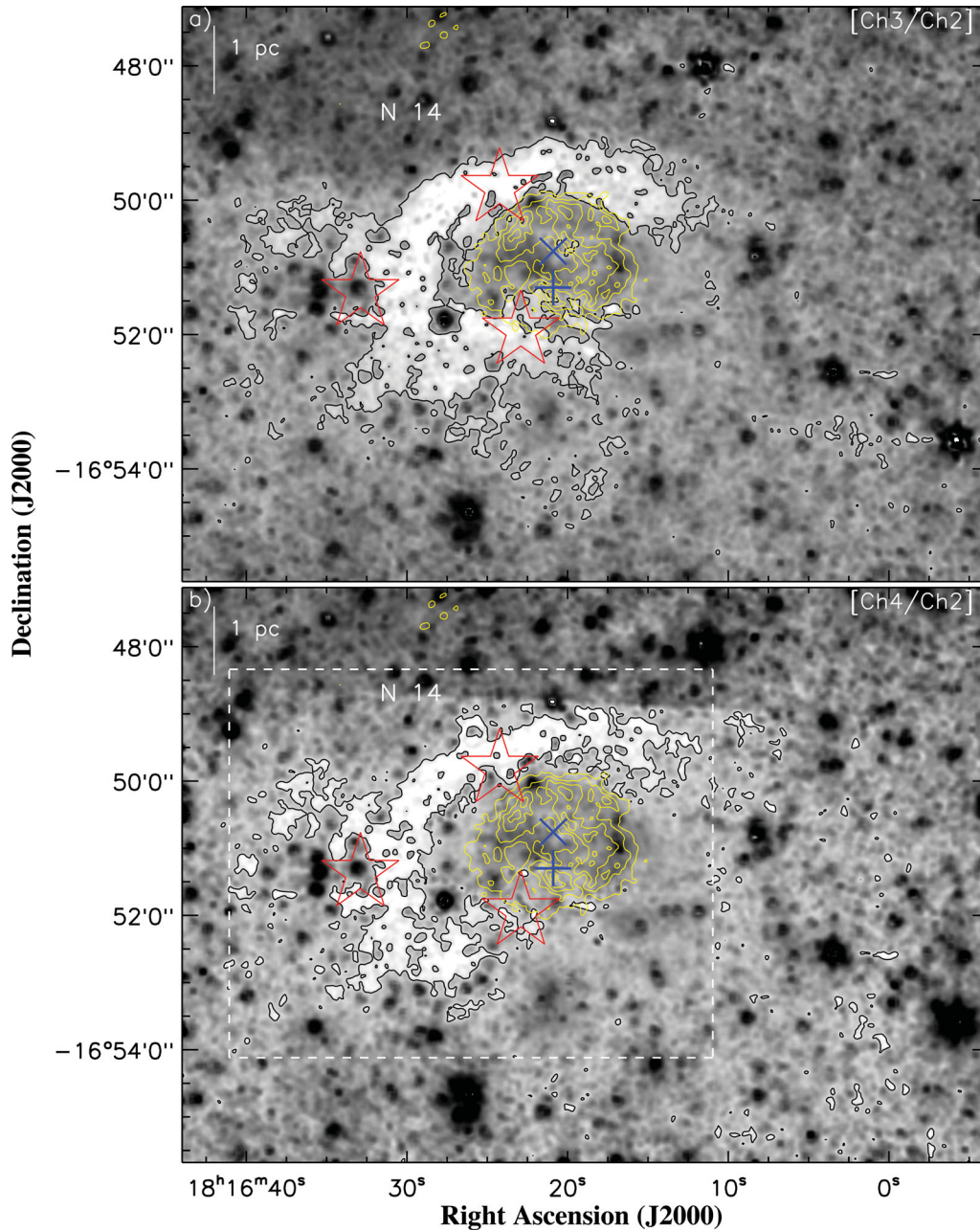


Figure 3. (a) GLIMPSE Ch3/Ch2 ratio map of the region around N14 (similar area as shown in Fig. 1). The ratio Ch3/Ch2 value is found to be ‘7–8’ and ‘8.5–10’ in the bubble interior and for the brightest part of the PDR, respectively. The Ch3/Ch2 ratio contours are also overlaid on the image with a level of 8.3, a representative value between ‘7’ and ‘8.5’. (b) The Ch4/Ch2 ratio map of the region is shown here. The ratio Ch4/Ch2 value for the brightest part of the PDR and the interior is ‘30–34’ and ‘23–25’, respectively. The Ch4/Ch2 ratio contours are also overlaid on the image with a level of 27.8, a representative value between ‘25’ and ‘30’. The white dashed box is shown as a zoomed-in view in Fig. 4. MAGPIS 20 cm radio contours in yellow colour are also overlaid in both the figures. The marked symbols and levels of radio contours on the image are similar to those shown in Fig. 1.

environment (Povich et al 2007). The IRAC bands contain a number of prominent atomic and molecular lines/features such as H₂ lines in all channels (see table 1 from Smith & Rosen 2005), Br α 4.05 μ m (Ch2), Fe II 5.34 μ m (Ch3), Ar II 6.99 μ m and Ar III 8.99 μ m (Ch4) (see Reach et al. 2006). We know that the *Spitzer*-IRAC bands, Ch1, Ch3 and Ch4, contain the PAH features at 3.3, 6.2, 7.7 and 8.6 μ m, whereas Ch2 (4.5 μ m) does not include any PAH features. Therefore, IRAC ratio (Ch4/Ch2, Ch3/Ch2 and Ch1/Ch2) maps are being used to trace out the PAH features in massive star-

forming regions (e.g. Povich et al 2007; Watson et al. 2008; Kumar & Anandarao 2010; Dewangan et al. 2012) due to UV radiation from massive star(s). In order to make the ratio maps, we generate residual frames for each band removing point sources by choosing an extended aperture (12.2 arcsec) and a larger sky annulus (14.6–24.4 arcsec; Reach et al. 2005) in the IRAF/DAOPHOT software (Stetson 1987). These residual frames are then subjected to median filtering with a width of 4 pixels and smoothing by 9 \times 9 pixels using the boxcar algorithm. Figs 3(a) and (b) represent the IRAC

ratio maps, Ch3/Ch2 and Ch4/Ch2, around the bubble N14, respectively. The ratio contours are also overlaid on the maps for better clarity and insight (see Fig. 3). Both the ratio maps clearly trace the prominent PAH emissions and subsequently the extent of PDRs in the region. The IRAC ratio maps reveal that the bubble is traced by the PAH emission following an almost circular morphology except in south-west direction towards the low molecular density environment, which was also reported by Deharveng et al. (2010).

The emission contours of dust (ATLASGAL 870 μm and BOLOCAM 1.1 mm) and molecular gas (JCMT CO 3–2) exhibit the evidence of collected material along the bubble (see Figs 1–3). Deharveng et al. (2010) tabulated the positions of three 870 μm dust condensations with their respective molecular velocities using the $\text{NH}_3(1,1)$ inversion line between 39 and 41.5 km s^{-1} . These values are also consistent with Beaumont & Williams (2010), who also reported velocity for the bubble N14 ($\sim 40.3 \text{ km s}^{-1}$). These velocity ranges of molecular gas are also compatible with the ionized gas velocity ($\sim 36 \text{ km s}^{-1}$) obtained by the hydrogen recombination line study around the H II region (Lockman 1989), which confirms the physical association of the molecular material and the H II region. It is also to be noted that the peaks of cold dust and molecular gas emission at different locations possibly indicate the fragmentation of collected materials into different individual clumps around the bubble. The evidence of collected material along the bubble is further confirmed by the detection of the H_2 emission (see Fig. 4). Fig. 4 represents the continuum-subtracted H_2 image at 2.12 μm and reveals that the H_2 emission surrounds the H II region along the bubble, forming a PDR, which may be collected due to the shock. In brief, the PAH emission, cold dust emission, molecular CO gas and shocked H_2 emissions are coincident along the bubble.

3.3 Photometric analysis of point-like sources towards N14

In order to trace ongoing star formation activity around the bubble N14, we have identified YSOs using NIR and GLIMPSE data.

3.3.1 Selection of YSOs

We have used Gutermuth et al. (2009) criteria based on four IRAC bands to identify YSOs and various possible contaminants (e.g. broad-line AGNs, PAH-emitting galaxies, shocked emission blobs/knots and PAH-emission-contaminated apertures). These YSOs are further classified into different evolutionary stages (i.e. Class I, Class II, Class III and photospheres) using slopes of the IRAC spectral energy distribution (SED). Fig. 5(a) shows the IRAC colour–colour ([3.6]–[4.5] versus [5.8]–[8.0]) diagram for all the identified sources. We find 33 YSOs (15 Class 0/I; 18 Class II), 621 photospheres and 78 contaminants in the selected region around the bubble N14. The details of YSO classifications can be found in Dewangan & Anandarao (2011). We have also applied criteria ([3.6]–[4.5] = 0.7 and [4.5]–[5.8] = 0.7; Hartmann et al. 2005; Getman et al. 2007) to identify protostars (Class I) among the sources, which are detected in three IRAC/GLIMPSE bands, but not in the 8.0 μm band, and rest of the remaining sources are subjected to SED criteria (see Dewangan & Anandarao 2011) to select the Class II and Class III sources. We identify 186 additional YSOs (10 Class 0/I; 176 Class II) through the colour–colour diagram using three GLIMPSE bands in the region (see Fig. 5 b).

GLIMPSE 3.6 and 4.5 μm bands are more sensitive for point sources than GLIMPSE 5.8 and 8.0 μm images. Therefore, a larger number of YSOs can be identified using a combination of UKIDSS NIR HK_s photometry with GLIMPSE 3.6 and 4.5 μm (i.e. NIR-IRAC) photometry, where sources are not detected in the IRAC

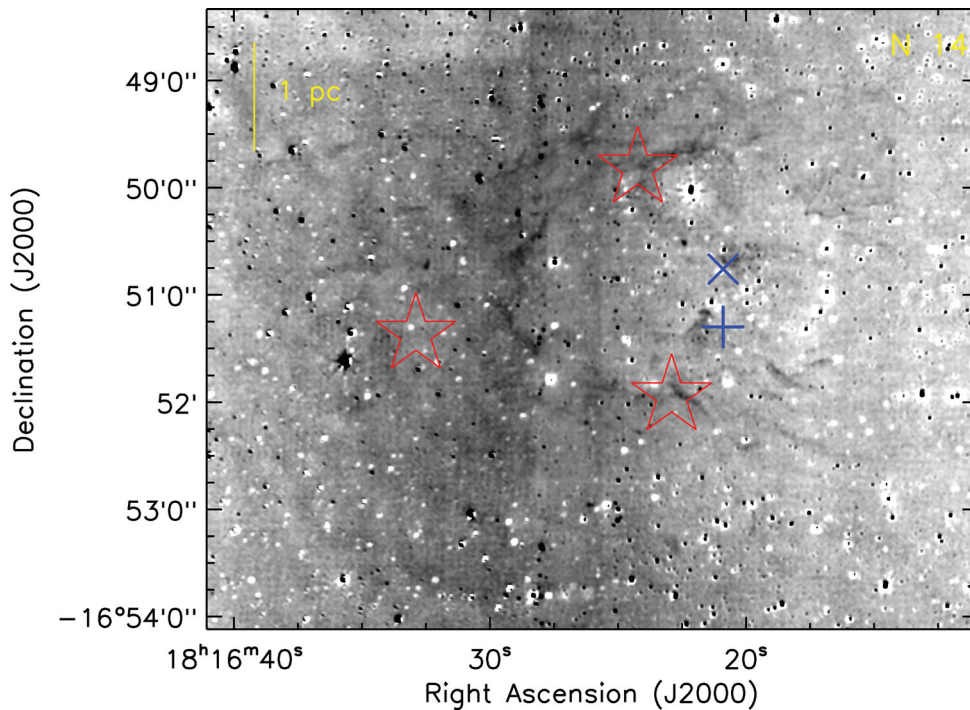


Figure 4. Zoomed-in inverted grey-scale continuum-subtracted H_2 image at 2.12 μm around N14 (size $\sim 7.2 \times 5.7 \text{ arcmin}^2$; as shown by a dashed box in Fig. 3 b). The H_2 image clearly indicates the detected H_2 emission (dark features as seen in GLIMPSE images) in the selected region around N14. The marked symbols are similar to those shown in Fig. 1. The continuum-subtracted H_2 image is processed through median filtering with a width of 4 pixels and smoothed by 4×4 pixels using the boxcar algorithm to trace the faint features in the image.

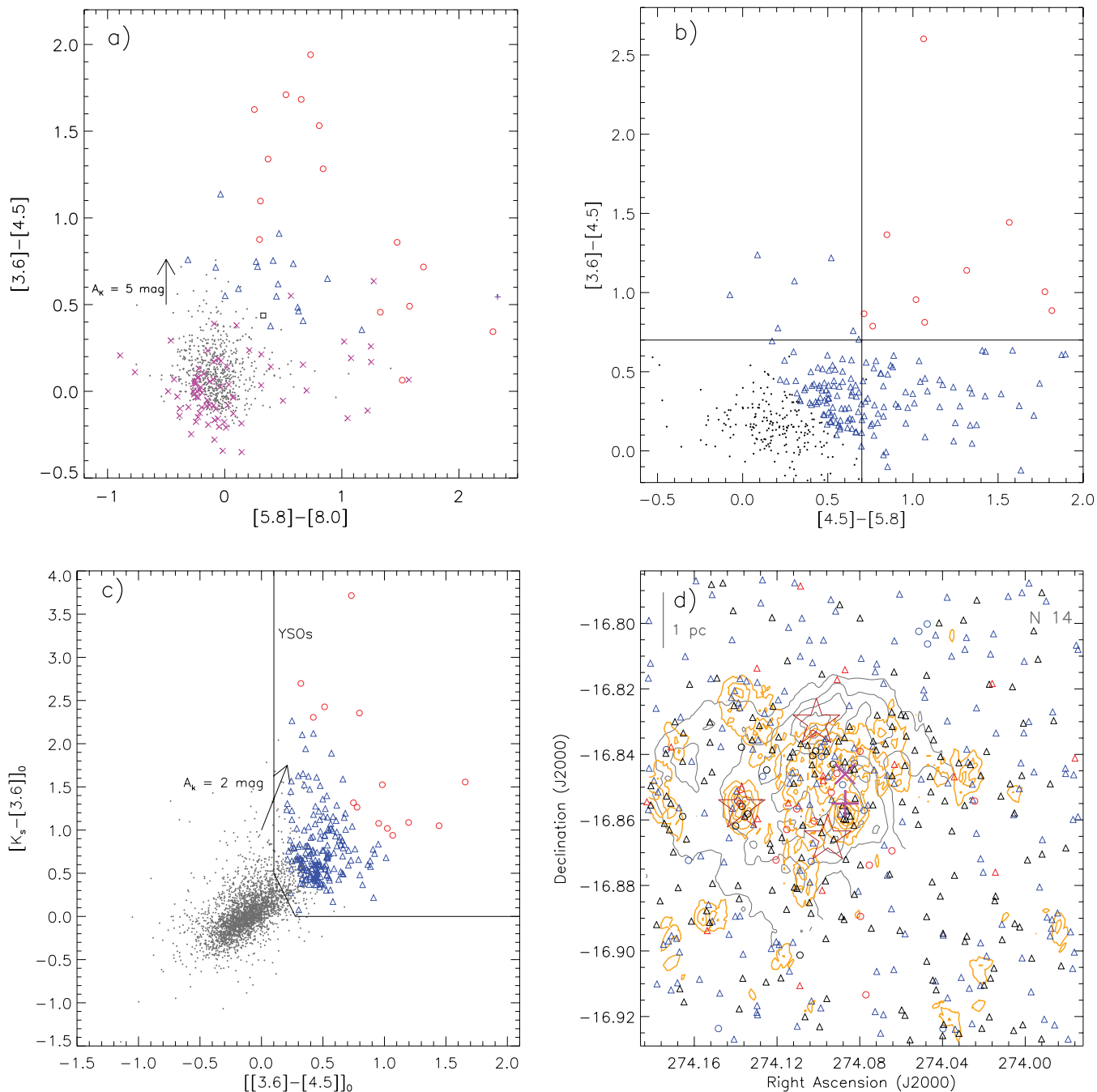


Figure 5. (a) Colour–colour diagram (CC-D) using *Spitzer*-IRAC four bands for all the sources identified within the region shown in Fig. 1. The extinction vector for $A_K = 5$ mag is shown by an arrow, using the average extinction law from Flaherty et al. (2007). The dots in grey colour around the centre (0,0) locate the stars with only photospheric emissions. The open squares (black), open triangles (blue) and open circles (red) represent the Class III, Class II and Class 0/I sources, respectively, classified using the α_{IRAC} criteria. The ‘x’ symbols in magenta colour show the identified PAH-emission-contaminated apertures in the region. The PAH galaxy contamination source is also marked by a violet cross (+) symbol in the diagram (see the text). (b) CC-D of the sources detected in three IRAC/GLIMPSE bands, except 8.0 μm . The small filled circles (black), open triangles (blue) and open circles (red) represent the Class III, Class II and Class 0/I sources, respectively (see the text for the YSO selection criteria). (c) The figure shows the de-reddened the $[K_s - [3.6]]_0$ versus $[[3.6] - [4.5]]_0$ CC-D using NIR and GLIMPSE data. The selected region shown by the solid lines represents the location of YSOs. The extinction vector for $A_K = 2$ mag is shown by an arrow, calculated using the average extinction law from Flaherty et al. (2007). The open red circles and open blue triangles represent the Class I and Class II sources, respectively. (d) The plot represents the spatial distribution of all identified YSOs in the selected region around N14. The YSO surface density contours are plotted for 6, 9, 14, 20 and 26 YSOs pc^{-2} , from the outer to the inner side (see the text for details). The open circles and open triangles show the Class I and Class II sources, respectively. The YSOs identified using four IRAC, three IRAC and NIR-IRAC data are shown by red, black and blue colours, respectively. The JCMT ^{12}CO (3–2) contours in grey colour and marked symbols are similar to those shown in Fig. 1.

5.8 and/or 8.0 μm band (Gutermuth et al. 2009). We followed the criteria given by Gutermuth et al. (2009) to identify YSOs using H , K_s , 3.6 and 4.5 μm data. We have found 199 additional YSOs (185 Class II and 14 Class I) using NIR-IRAC data (see Fig. 5 c).

Finally, we have obtained a total of 418 YSOs (379 Class II and 39 Class I) using NIR and GLIMPSE data in the region.

3.3.2 Spatial distribution of YSOs

To study the spatial distribution of YSOs, we generated the surface density map of all YSOs using a 5 arcsec grid size, following the same procedure as given in Gutermuth et al. (2009). The surface density map of YSOs is constructed using six nearest-neighbour (NN) YSOs for each grid point. Fig. 5(d) shows the spatial distribution of all identified YSOs (Class I and Class II) in the region. The contours of YSO surface density are also overlaid on the map. The levels of YSO surface density contours are 6 (2.1σ), 9 (3.2σ), 14 (4.9σ), 20 (7.0σ) and 26 (9.1σ) YSOs pc^{-2} , increasing from the outer to the inner region. We have also calculated the empirical cumulative distribution (ECD) as a function of the NN distance to identify the clustered YSOs in the region. Using the ECD, we estimate the distance of inflection $d_c = 0.54 \text{ pc}$ (0.0088 at 3.5 kpc) for the region for a surface density of 6 YSOs pc^{-2} (see Dewangan & Anandarao 2011, for details of d_c and ECD). We find that about 23 per cent (98 out of 418) YSOs are present in clusters. Fig. 5(d) reveals that the distribution of YSOs is mostly concentrated in and around the bubble, having the peak density of about 20 YSOs pc^{-2} (see also Fig. 6), while the YSO density of about 8 YSOs pc^{-2} (2.8σ) is also seen around the east and west regions close to the low density molecular gas and dust emission (see Fig. 6). It is also to be noted that the YSO clustering is seen along the PDR, at the borders of the bubble. The correlation of cold dust, molecular gas,

ionized gas and YSO surface density is shown in Fig. 6. The association of YSOs with the collected materials around the region further reveals the ongoing star formation at the borders of the bubble.

In addition, we have checked the possibility of intrinsically ‘red sources’ contamination, such as asymptotic giant branch (AGB) stars in our YSO sample. Recently, Robitaille et al. (2008) prepared an extensive catalogue of such red sources based on the *Spitzer* GLIMPSE and MIPS GAL surveys. They showed that two classes of sources are well separated in the $[8.0-24.0]$ colour space such that YSOs are redder than AGB stars in this space (see also Whitney et al. 2008). First, we applied red source criteria for all our selected YSOs having 4.5 and 8.0 μm detections. We found 19 out of 33 YSOs (~ 57 per cent) as possible intrinsically ‘red sources’ and then further utilized $[8.0-24.0]$ colour space to identify the AGB contaminations from selected ‘red sources’. We have taken the MIPS 24 μm magnitude for our selected sources from Robitaille et al. (2008), wherever it is available, and also extracted a few more sources from the archival MIPS GAL 24 μm image. We performed aperture photometry on the MIPS GAL 24 μm image using IRAF with a 7 arcsec aperture and a sky annulus from 7 to 13 arcsec. Zero-points and aperture corrections were adopted from *MIPS Instrument Handbook* Version 3, 2011 March, for selected aperture. The MIPS 24 μm image is saturated close to the IRAS position; however, a few point sources are seen around the bubble. Therefore, we obtained MIPS 24 μm magnitudes for only nine YSOs (seven Class I and two Class II) identified as red sources. Finally, we identified two likely AGB contaminations out of nine red sources, following the criteria suggested by Robitaille et al. (2008), which are located away from the identified YSO clusters (see Fig. 6). We have not considered these likely AGB contaminations for further analysis.

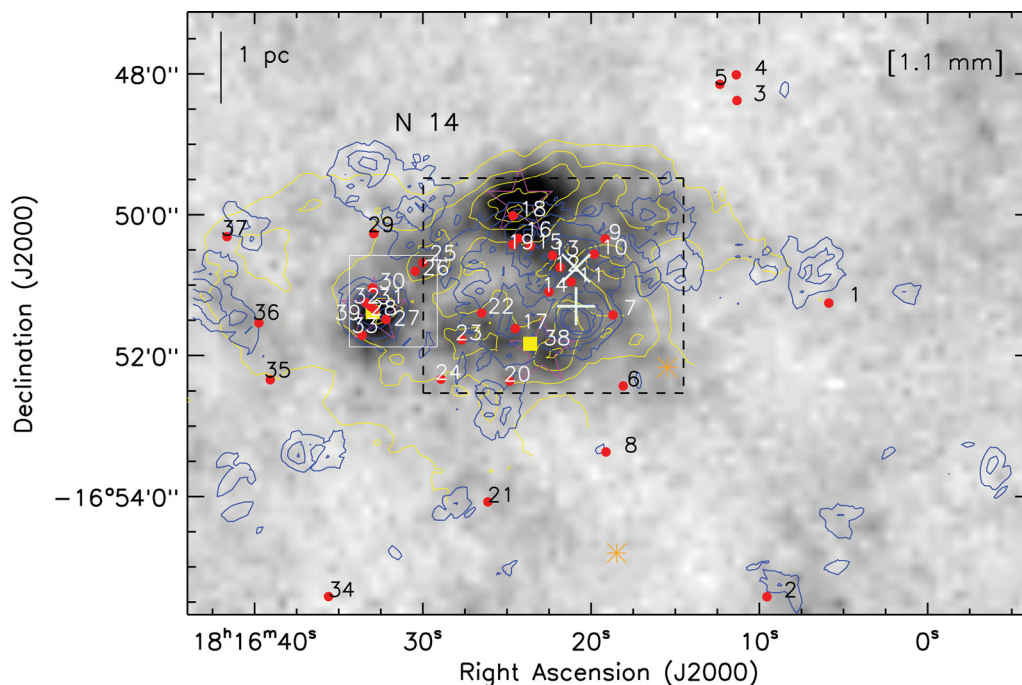


Figure 6. The spatial distribution of YSOs, dust emission and molecular gas in the selected region around N14. The BOLOCAM 1.1 mm image is overlaid with contours of YSO surface density (blue; similar levels as presented in Fig. 5 d) and JCMT CO 3–2 (yellow; similar levels as shown in Fig. 1) data. All Class I YSOs (see subsection 3.3.3) are also marked (red circles) and labelled as 1, . . . , 37 on the image (see Table 1). Two selected sources (s38 and s39) are shown by filled yellow squares and labelled, which are associated with the peaks of molecular gas and dust emission around the bubble. The position of two likely AGB contaminations is also marked by orange asterisks on the image. Two boxes are shown as a zoomed-in view in Fig. 7.

3.3.3 SED modelling of Class I YSOs

In this subsection, we present SED modelling of all 37 identified Class I YSOs (designated as s1, . . . , s37) as well as two selected YSOs (s38 and s39) associated with the peak of molecular gas and dust clumps around the bubble, in our selected region around N14, to derive their various physical parameters using an online SED modelling tool (Robitaille et al. 2006, 2007). It is interesting to note that ‘s39’ is a deeply embedded source (prominently seen in the 24 μm image), detected only in 5.8 μm and longer wavelength bands. NIR and *Spitzer* IRAC/GLIMPSE photometric magnitudes for these selected YSOs are listed in Table 1 along with IRAC spectral indices (α_{IRAC}) and are also labelled in Fig. 6. *Spitzer* 24 μm magnitudes are also listed for selected YSOs, wherever it is available. Figs 7(a) and (b) show the zoomed-in three-colour composite image using GLIMPSE [5.8 μm (red) and 4.5 μm (green)] and UKIDSS K_s (blue) around the east of the bubble close to the peak of a dense clump and around the bubble, respectively. Fig. 7(a) clearly exhibits the location of a deeply embedded source ‘s39’ along with other identified Class I sources close to the peak of a cold dust emission. Fig. 7(b) presents the zoomed-in view around the bubble with the positions of a few identified YSOs (such as s17, s18 and s38, along with other identified Class I YSOs).

IRAC spectral indices were calculated using a least-squares fit to the IRAC flux points in a $\log(\lambda)$ versus $\log(\lambda F_\lambda)$ diagram for those sources that are detected in at least three IRAC bands (see Dewangan & Anandarao 2011, for details). The SED model tool requires a minimum of three data points with good quality as well as the distance to the source and visual extinction value. These models assume an accretion scenario with a central source associated with a rotationally flattened infalling envelope, bipolar cavities and a flared accretion disc, all under radiative equilibrium. The model grid consists of 20 000 models of two-dimensional Monte Carlo simulations of radiation transfer with 10 inclination angles, resulting in a total of 200 000 SED models. The grid of SED models covers the mass range from 0.1 to 50 M_\odot . Only those models are selected that satisfy the criterion $\chi^2 - \chi_{\text{best}}^2 < 3$, where χ^2 is taken per data point. The plots of SED fitted models are shown in Fig. 8 for 9 out of 39 selected YSOs associated with the molecular and dust clumps. The weighted mean values of the physical parameters (mass and luminosity) along with the standard deviations derived from the SED modelling for all the selected sources are given in Table 1. The SED results clearly show that the YSOs having higher luminosity represent more massive candidates. The table also contains the number of models that satisfy the χ^2 criterion as mentioned above. The derived SED model parameters show that the average values of mass and luminosity of the 39 selected sources are about 4.8 M_\odot and 1817.1 L_\odot , respectively. Our SED result shows that the source ‘s4’ is the most luminous and massive YSO ($\sim 20.5 M_\odot$) among all selected YSOs away from the bubble and is saturated in the GLIMPSE 8 μm image. It is however tabulated as an OH selected AGB/post-AGB candidate by Sevenster (2002) using the 1612 MHz masing OH line profile. The YSO surface density contours clearly trace a clustering of Class I YSOs (s27–28, s30–33 and s39) with ~ 20 YSOs pc^{-2} associated with the dense dust clump at the eastern border of the bubble N14 along with other peaks of YSO surface density (see Figs 6, 7 a and Table 1). It is found that about 5 young massive embedded YSOs (s6, s18, s23, s28 and s31) with a mass range of 8–10 M_\odot and about 15 intermediate mass YSOs (s7, s9–10, s12, s14, s16–17, s19, s22, s25–26, s30, s33, s38–39) with a mass range of 3–7 M_\odot are associated with the molecular and dust fragmented clumps at the borders of the bubble (see Figs 6, 7 and Table 1).

It is interesting to note that the sources s18, s28, s31, s38 and s39 are associated with the peak of dust clumps at the border of the bubble and three of them (s18, s28 and s31) are possibly young massive protostars. Finally, the SED modelling results favour ongoing star formation around the region with detection of YSOs as well as some massive protostars in their early phase of formation.

Recently, Kryukova et al. (2012) studied a relationship between bolometric luminosity and MIR luminosity (integrated from 1.25 to 24 μm) of *Spitzer* identified protostars in nine nearby molecular clouds, independent of SED modelling. We have also computed the MIR luminosity (L_{MIR}) of our selected sources from integrating the SED using their available photometric infrared data (see Table 1 for L_{MIR}). However, the estimated MIR luminosity of our selected sources is underestimated because of the lack of 24 μm and longer wavelength data for most of the sources. Therefore, we prefer to use model derived SED physical parameters (like mass and luminosity) over luminosity derived independently of SED modelling for our selected sources. It is known that the physical parameters obtained from SED modelling are not unique but indicative. We therefore used only masses of the selected sources for their relative comparison in terms of mass.

3.3.4 Ionizing candidates

The presence of both PAH emission around the bubble and radio emission inside the bubble clearly suggests the presence of the ionizing source(s) with UV radiation close to the centre of the bubble. One can find more details regarding identification of ionizing candidate(s) inside the bubble in Pomarés et al. (2009) and Ji et al. (2012). It is to be noted that no ionizing stars are reported for this bubble. Beaumont & Williams (2010) listed about six O9.5 stars to produce the observed 20 cm integrated flux (~ 2.41 Jy) for the H II region associated with the bubble N14. Therefore, we followed suggestions of Pomarés et al. (2009) and Ji et al. (2012) to trace the ionizing candidate(s) inside the bubble N14 using 2MASS and GLIMPSE photometric magnitudes. We selected eight candidates (designated as #1, . . . , #8) to search for O-type star(s) inside the bubble based on their detections in the *J* band to 5.8 μm or longer wavelength bands (see Fig. 7 b and Table 2). All selected candidates are marked and labelled in Fig. 7(b). We calculated the absolute JHK_s magnitude for each candidate using their 2MASS apparent *J*, *H* and K_s magnitudes. 2MASS photometry is used here due to nonavailability of GPS *J*-band photometry. We used a distance of 3.5 kpc and estimated the extinction for each source from the NIR colour–colour diagram (CC-D). We followed the extinction law given by Indebetouw et al. (2005) ($A_J/A_V = 0.284$, $A_H/A_V = 0.176$ and $A_K/A_V = 0.114$) and used the intrinsic colours $(J - H)_0 (= -0.11)$ and $(H - K)_0 (= -0.10)$ obtained from Martins & Plez (2006). We compared the derived absolute JHK_s magnitudes with those listed by Martins & Plez (2006) for our selected candidates, and found two O-type candidates (#4 and #6) inside the bubble. We also checked their evolutionary stages using CC-D (see subsection 3.3.1) and found that all the sources are the main-sequence stars except source #3, which is identified as a Class I YSO and designated as s14 in Table 1. The positions of the eight selected candidates are tabulated in Table 2 with their 2MASS NIR and GLIMPSE apparent magnitudes, calculated visual extinction, estimated absolute JHK_s magnitudes and the possible spectral class obtained from the comparison of the absolute magnitude of each candidate with the listed values of Martins & Plez (2006).

Table 1. NIR, *Spitzer* IRAC/GLIMPSE and MIPS 24 μm photometric magnitudes are listed for all selected YSOs in the region around the bubble (see the text). The spectral index (α_{IRAC}) of sources was obtained having the magnitude of at least three IRAC wavelengths. The MIR luminosity (L_{MIR}) of selected sources was obtained by integrating the SED using the available photometric infrared data. The weighted mean of luminosity (L_*) and mass (M_*) along with the number of models of all selected sources are also listed in the table, which are obtained by SED modelling (see the text).

Source	RA (2000)	Dec. (2000)	J (mag)	H (mag)	K_s (mag)	[3.6] (mag)	[4.5] (mag)	[5.8] (mag)	[8.0] (mag)	[24.0] (mag)	α_{IRAC}	L_{MIR} (L_{\odot})	L_* (L_{\odot})	M_* (M_{\odot})	No. of models
s1	18:16:05.87	-16:51:15.3	-	-	-	14.27 \pm 0.19	12.33 \pm 0.11	10.45 \pm 0.07	9.72 \pm 0.09	-	2.45	0.97	252.66 \pm 7.42	5.43 \pm 4.25	1331
s2	18:16:09.55	-16:55:25.5	-	14.66 \pm 0.01	14.34 \pm 0.01	14.10 \pm 0.10	13.30 \pm 0.16	-	-	-	-	0.54	4.53 \pm 4.72	1.51 \pm 1.17	6763
s3	18:16:11.33	-16:48:22.6	-	14.55 \pm 0.01	14.23 \pm 0.01	14.03 \pm 0.09	12.75 \pm 0.07	-	-	-	-	0.62	97.25 \pm 2.04	3.78 \pm 1.41	104
s4	18:16:11.37	-16:48:00.7	-	16.89 \pm 0.05	11.92 \pm 0.00	5.61 \pm 0.05	4.17 \pm 0.08	3.52 \pm 0.04	-	-	1.13	551.42	48 662.94 \pm 1.37	20.46 \pm 3.54	44
s5	18:16:12.35	-16:48:08.8	-	13.28 \pm 0.00	12.92 \pm 0.00	12.12 \pm 0.03	11.34 \pm 0.04	-	-	-	-	2.18	34.29 \pm 4.34	2.78 \pm 1.64	5334
s6	18:16:18.09	-16:52:25.7	-	-	13.21 \pm 0.07	10.51 \pm 0.20	10.44 \pm 0.12	7.26 \pm 0.05	5.74 \pm 0.09	2.14	3.28	36.39	1835.19 \pm 1.12	8.98 \pm 0.15	2
s7	18:16:18.71	-16:51:25.5	-	17.10 \pm 0.06	15.46 \pm 0.04	14.43 \pm 0.18	13.25 \pm 0.14	-	-	-	-	0.17	95.50 \pm 2.88	3.45 \pm 1.31	192
s8	18:16:19.12	-16:53:22.0	-	-	-	10.07 \pm 0.06	8.79 \pm 0.06	7.57 \pm 0.05	6.73 \pm 0.05	3.82	1.03	19.20	532.61 \pm 2.51	5.03 \pm 1.78	79
s9	18:16:19.17	-16:50:20.6	-	14.84 \pm 0.09	13.73 \pm 0.06	11.83 \pm 0.07	11.11 \pm 0.07	10.40 \pm 0.11	8.70 \pm 0.03	-	0.72	2.75	122.35 \pm 3.73	3.78 \pm 1.71	908
s10	18:16:19.81	-16:50:33.7	-	16.74 \pm 0.04	14.69 \pm 0.02	11.44 \pm 0.10	10.70 \pm 0.14	9.25 \pm 0.12	-	-	1.37	2.32	263.30 \pm 3.46	4.85 \pm 2.15	1253
s11	18:16:21.18	-16:50:57.3	-	14.64 \pm 0.01	13.50 \pm 0.01	12.83 \pm 0.11	11.84 \pm 0.06	-	-	-	-	0.96	38.41 \pm 3.70	2.98 \pm 1.82	612
s12	18:16:21.85	-16:50:44.9	-	-	-	12.15 \pm 0.06	11.05 \pm 0.07	10.20 \pm 0.07	9.89 \pm 0.19	-	-0.26	1.50	137.40 \pm 2.59	4.55 \pm 1.94	1358
s13	18:16:22.29	-16:50:34.7	-	-	-	13.17 \pm 0.08	12.36 \pm 0.16	11.29 \pm 0.22	-	-	0.77	0.39	46.25 \pm 4.21	2.87 \pm 2.11	10000
s14	18:16:22.51	-16:51:05.8	13.07 \pm 0.03	11.84 \pm 0.02	11.32 \pm 0.02	10.77 \pm 0.09	10.43 \pm 0.12	9.68 \pm 0.12	7.39 \pm 0.06	-	1.05	14.79	138.00 \pm 1.88	4.33 \pm 1.33	71
s15	18:16:22.62	-16:50:26.4	-	15.34 \pm 0.01	14.15 \pm 0.01	12.87 \pm 0.12	12.08 \pm 0.08	-	-	-	-	0.63	24.30 \pm 3.02	2.41 \pm 1.37	7464
s16	18:16:24.32	-16:50:20.2	-	-	-	12.18 \pm 0.17	11.17 \pm 0.13	9.40 \pm 0.11	-	-	-	2.52	492.39 \pm 4.20	6.28 \pm 3.31	3801
s17	18:16:24.50	-16:51:37.1	-	-	-	10.55 \pm 0.02	10.06 \pm 0.02	9.05 \pm 0.09	7.47 \pm 0.11	1.83	0.78	20.14	170.49 \pm 1.92	4.66 \pm 1.33	312
s18	18:16:24.65	-16:50:00.9	-	-	-	9.55 \pm 0.10	7.84 \pm 0.06	6.65 \pm 0.06	6.13 \pm 0.09	0.59	1.05	76.03	953.65 \pm 2.89	7.28 \pm 2.95	14
s19	18:16:24.66	-16:50:25.4	-	-	-	13.09 \pm 0.11	12.20 \pm 0.09	10.38 \pm 0.18	-	-	2.38	0.64	173.07 \pm 3.01	4.34 \pm 2.21	1985
s20	18:16:24.84	-16:52:21.5	-	14.58 \pm 0.01	14.16 \pm 0.01	14.21 \pm 0.29	13.07 \pm 0.15	-	-	-	-	0.60	6.52 \pm 4.66	1.65 \pm 1.23	4776
s21	18:16:26.13	-16:54:04.5	-	-	-	13.98 \pm 0.12	13.02 \pm 0.18	12.01 \pm 0.22	-	-	0.94	0.20	20.91 \pm 4.46	2.11 \pm 1.96	10000
s22	18:16:26.51	-16:51:23.8	-	-	13.55 \pm 0.05	10.74 \pm 0.05	10.29 \pm 0.06	9.70 \pm 0.13	8.37 \pm 0.06	-	-0.12	4.33	595.87 \pm 3.31	6.97 \pm 2.09	15
s23	18:16:27.67	-16:51:46.5	-	-	-	6.70 \pm 0.00	5.83 \pm 0.00	4.58 \pm 0.00	4.28 \pm 0.00	-	0.06	236.40	8286.71 \pm 1.48	10.83 \pm 1.68	125
s24	18:16:28.92	-16:52:20.0	-	-	-	12.62 \pm 0.07	10.94 \pm 0.07	9.56 \pm 0.06	8.90 \pm 0.11	-	1.43	2.38	65.29 \pm 1.57	1.97 \pm 0.77	6
s25	18:16:29.99	-16:50:41.1	-	-	-	12.52 \pm 0.14	11.08 \pm 0.16	9.52 \pm 0.03	-	-	2.93	1.45	109.25 \pm 2.21	3.02 \pm 1.42	2068
s26	18:16:30.46	-16:50:48.1	-	15.86 \pm 0.02	13.81 \pm 0.01	11.87 \pm 0.09	10.96 \pm 0.08	10.48 \pm 0.17	-	-	-0.20	1.47	100.25 \pm 2.47	3.66 \pm 1.26	4548
s27	18:16:32.19	-16:51:29.3	-	-	-	13.02 \pm 0.07	12.15 \pm 0.09	11.44 \pm 0.12	-	-	0.17	0.41	47.17 \pm 2.37	2.77 \pm 1.01	10000
s28	18:16:32.86	-16:51:21.1	-	-	-	14.16 \pm 0.14	11.56 \pm 0.16	10.49 \pm 0.10	-	-	4.12	0.65	5310.55 \pm 2.63	10.67 \pm 2.45	65
s29	18:16:32.92	-16:50:16.2	-	-	-	13.90 \pm 0.16	12.76 \pm 0.14	11.45 \pm 0.22	-	-	1.87	0.28	56.93 \pm 4.69	2.88 \pm 2.23	9071
s30	18:16:33.00	-16:51:02.5	-	-	13.67 \pm 0.03	11.93 \pm 0.07	11.07 \pm 0.07	10.45 \pm 0.11	8.97 \pm 0.08	-	0.48	2.24	77.69 \pm 3.02	3.26 \pm 1.59	877
s31	18:16:33.09	-16:51:18.3	-	-	-	10.54 \pm 0.10	8.91 \pm 0.08	7.96 \pm 0.04	7.70 \pm 0.04	-	0.35	10.48	971.52 \pm 1.62	7.81 \pm 0.88	51
s32	18:16:33.38	-16:51:15.2	15.16 \pm 0.04	14.37 \pm 0.03	13.97 \pm 0.08	13.56 \pm 0.15	12.79 \pm 0.16	-	-	-	-	1.08	9.48 \pm 4.94	1.95 \pm 1.22	8747
s33	18:16:33.60	-16:51:42.7	-	-	-	13.81 \pm 0.10	12.45 \pm 0.10	11.60 \pm 0.14	-	-	1.38	0.29	118.41 \pm 7.00	4.24 \pm 3.11	4351
s34	18:16:35.60	-16:55:25.2	-	16.14 \pm 0.02	15.81 \pm 0.04	13.28 \pm 0.09	13.00 \pm 0.13	-	-	-	-	0.27	18.00 \pm 2.69	1.76 \pm 1.41	53
s35	18:16:39.07	-16:52:20.5	14.25 \pm 0.03	13.65 \pm 0.00	13.19 \pm 0.00	11.32 \pm 0.10	10.66 \pm 0.09	10.13 \pm 0.09	-	-	-0.55	3.57	92.18 \pm 2.87	3.41 \pm 1.14	247
s36	18:16:39.74	-16:51:32.2	-	-	-	13.15 \pm 0.08	12.36 \pm 0.09	11.59 \pm 0.17	10.89 \pm 0.27	-	-0.23	0.50	22.89 \pm 2.23	2.04 \pm 1.19	5010
s37	18:16:41.64	-16:50:18.7	-	14.53 \pm 0.01	15.02 \pm 0.02	13.52 \pm 0.08	13.32 \pm 0.13	-	-	-	-	0.54	58.42 \pm 1.41	4.28 \pm 0.36	4
s38	18:16:23.62	-16:51:50.0	-	-	-	9.81 \pm 0.02	9.18 \pm 0.01	7.75 \pm 0.05	-	1.95	1.13	20.74	597.35 \pm 2.50	5.43 \pm 1.73	1118
s39	18:16:32.99	-16:51:23.1	-	-	-	-	-	10.05 \pm 0.07	8.18 \pm 0.05	1.71	-	17.08	228.59 \pm 1.48	5.32 \pm 0.95	158

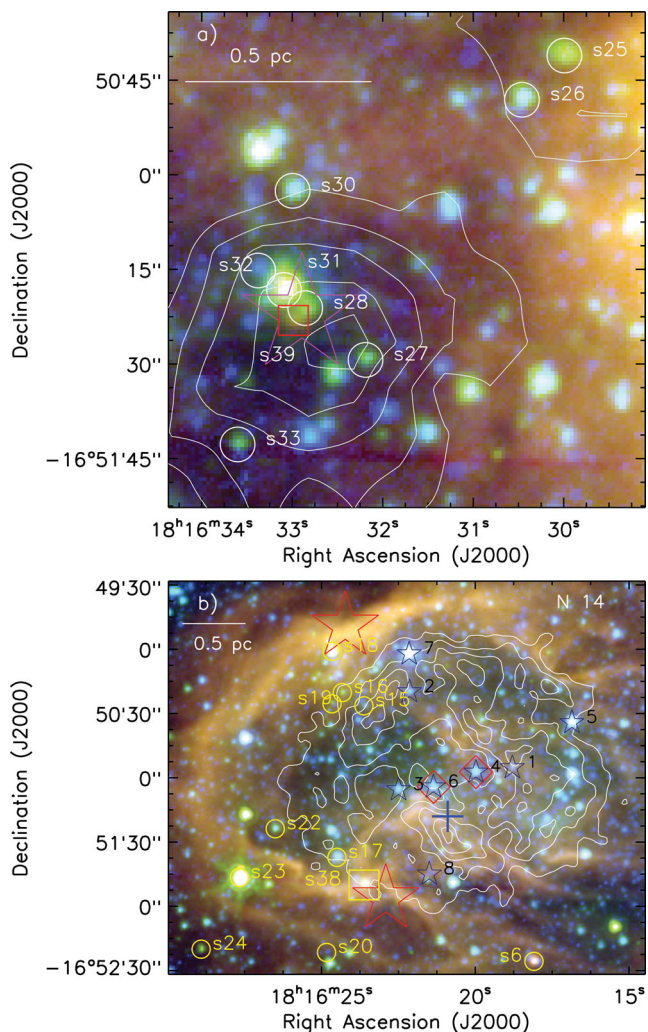


Figure 7. Three-colour composite image [UKIRT K_s (blue) and GLIMPSE 4.5 μm (green), 5.8 μm (red)] of the two zoomed-in regions around the bubble N14. (a) The figure clearly exhibits the location of a deeply embedded source ‘s39’ along with other identified Class I sources close to the peak of cold dust emission (see the white solid box in Fig. 6). (b) The MAGPIS 20 cm contours are overlaid on the zoomed-in region (dashed box in Fig. 6) with similar levels as shown in Fig. 2 close to the bubble N14 (size $\sim 3.7 \times 3.1$ arcmin 2). The eight selected main-sequence stars as probable ionizing candidates (see subsection 3.3.4) are also marked (black star symbols) and labelled as 1, . . . , 8 on the image (see Table 2). The diamonds in red colour are identified as the O-type ionizing stars (#4 and #6) inside the bubble. Some of Class I YSOs in yellow colour are also marked and labelled on the image.

3.4 Star formation scenario

We have found evidence of collected material along the bubble and also ongoing formation of YSOs at the borders of the bubble. The YSO clusters and embedded YSOs discovered are associated with the peak of molecular and cold dust material collected at the borders of the bubble. The morphology and distribution of YSOs suggest that the bubble N14 is a site of star formation possibly triggered by the expansion of the H II region. In recent years, the triggered star formation process, especially the ‘collect and collapse’ mechanism, has been studied extensively at the borders of many H II regions such as Sh 2-104, RCW 79, Sh 2-212, RCW 120, Sh 2-217, G8.14+0.23 (Deharveng et al. 2003, 2008, 2009; Zavagno et al. 2006, 2010;

Brand et al. 2011; Dewangan et al. 2012). In order to check the ‘collect and collapse’ process as the triggering mechanism around N14, we have calculated the dynamical age (t_{dyn}) of the H II region and compared it with an analytical model by Whitworth et al. (1994). We have estimated the age of the H II region at a given radius R , using the following equation (Dyson & Williams 1980):

$$t_{\text{dyn}} = \left(\frac{4 R_s}{7 c_s} \right) \left[\left(\frac{R}{R_s} \right)^{7/4} - 1 \right] \quad (1)$$

where c_s is the isothermal sound velocity in the ionized gas ($c_s = 10 \text{ km s}^{-1}$) and R_s is the radius of the Strömngren sphere, given by $R_s = (3N_{\text{uv}}/4\pi n_0^2 \alpha_B)^{1/3}$, where the radiative recombination coefficient $\alpha_B = 2.6 \times 10^{-13} (10^4 \text{ K T}^{-1})^{0.7} \text{ cm}^3 \text{ s}^{-1}$ (Kwan 1997). In this calculation, we have used $\alpha_B = 2.6 \times 10^{-13} \text{ cm}^3 \text{ s}^{-1}$ for the temperature of 10^4 K . N_v is the total number of ionizing photons per unit time emitted by ionizing stars and n_0 is the initial particle number density of the ambient neutral gas. We have adopted the Lyman continuum photon flux value ($N_{\text{uv}} =$) of $2.34 \times 10^{48} \text{ ph s}^{-1}$ ($\log N_{\text{uv}} = 48.36$) from Beaumont & Williams (2010) for an electron temperature, distance and integrated 20 cm (1.499 GHz) flux density of 10^4 K , 3.5 kpc and 2.41 Jy, respectively. We calculated the mean H $_2$ number density near the H II region using archival ^{12}CO zeroth moment map or column density map. In general, the zeroth moment map (in unit of K km s^{-1}) is created by integrating the brightness temperature over some velocity range. We derived the column density using the formula $N_{\text{H}_2} (\text{cm}^{-2}) = X \times W_{\text{CO}}$, assuming that the molecular clumps/cores are approximately spherical in shape. We used the CO–H $_2$ conversion factor (also called the X factor) for dense gas as $6 \times 10^{20} \text{ cm}^{-2} \text{ K}^{-1} \text{ km}^{-1} \text{ s}$ from Shetty et al. (2011). We find almost a closed circular structure of the integrated CO line emission (W_{CO}) (typical value of $\sim 23.43 \text{ K km s}^{-1}$) using the archival column density map, which traces well the bubble around the H II region. The mean H $_2$ number density is obtained to be 2071.5 cm^{-3} using the relation $N_{\text{H}_2} (\text{cm}^{-2})/L (\text{cm})$, where L is the molecular core size of about $6.79 \times 10^{18} \text{ cm}$ ($\sim 2.2 \text{ pc}$) near the H II region. The estimated mean H $_2$ number density could be underestimated because of not considering the fact that the ^{12}CO (3–2) transition can be (partly) optical thick in nature and also assuming a spherical structure in the calculation. Using N_{uv} , a radius of the H II region ($R =$) 2.48 pc, and $n_0 = 2071.5 \text{ cm}^{-3}$, we have obtained $t_{\text{dyn}} \sim 0.74 \text{ Myr}$ using equation (1). The time-scale of the H II region expansion is actually not an easy issue. There is a long-standing problem of the lifetime of Galactic ultra-compact (UC) H II regions. Wood & Churchwell (1989) observationally reported that the typical lifetime of UC H II regions is about 10^5 yr , but the lifetime of an expanding UC H II region (i.e. the time-scale to reach pressure equilibrium with the surrounding environment) is estimated to be about 10^4 yr , for the 10 km s^{-1} expansion velocity of ionized gas, with a typical radius of $\sim 0.1 \text{ pc}$. So, the difference between these time-scales is known as the lifetime problem of UC H II regions. This lifetime problem might have implications in the present case even if it is only the UC H II region which is living too long. Therefore, our estimated time-scale should be considered with a caution. Following the Whitworth et al. (1994) analytical model for the ‘collect and collapse’ process, we have estimated a fragmentation time-scale (t_{frag}) of 1.27–2.56 Myr for a turbulent velocity (a_s) of 0.2–0.6 km s^{-1} in the collected layer. We find that the dynamical age is smaller than the fragmentation time-scale for $n_0 = 2071.5 \text{ cm}^{-3}$. We have checked the variation of t_{frag} and t_{dyn} with initial density (n_0) of the ambient neutral medium and found that if t_{dyn} is larger than t_{frag} , then ambient density (n_0) should be larger than 3610, 5710, 6700

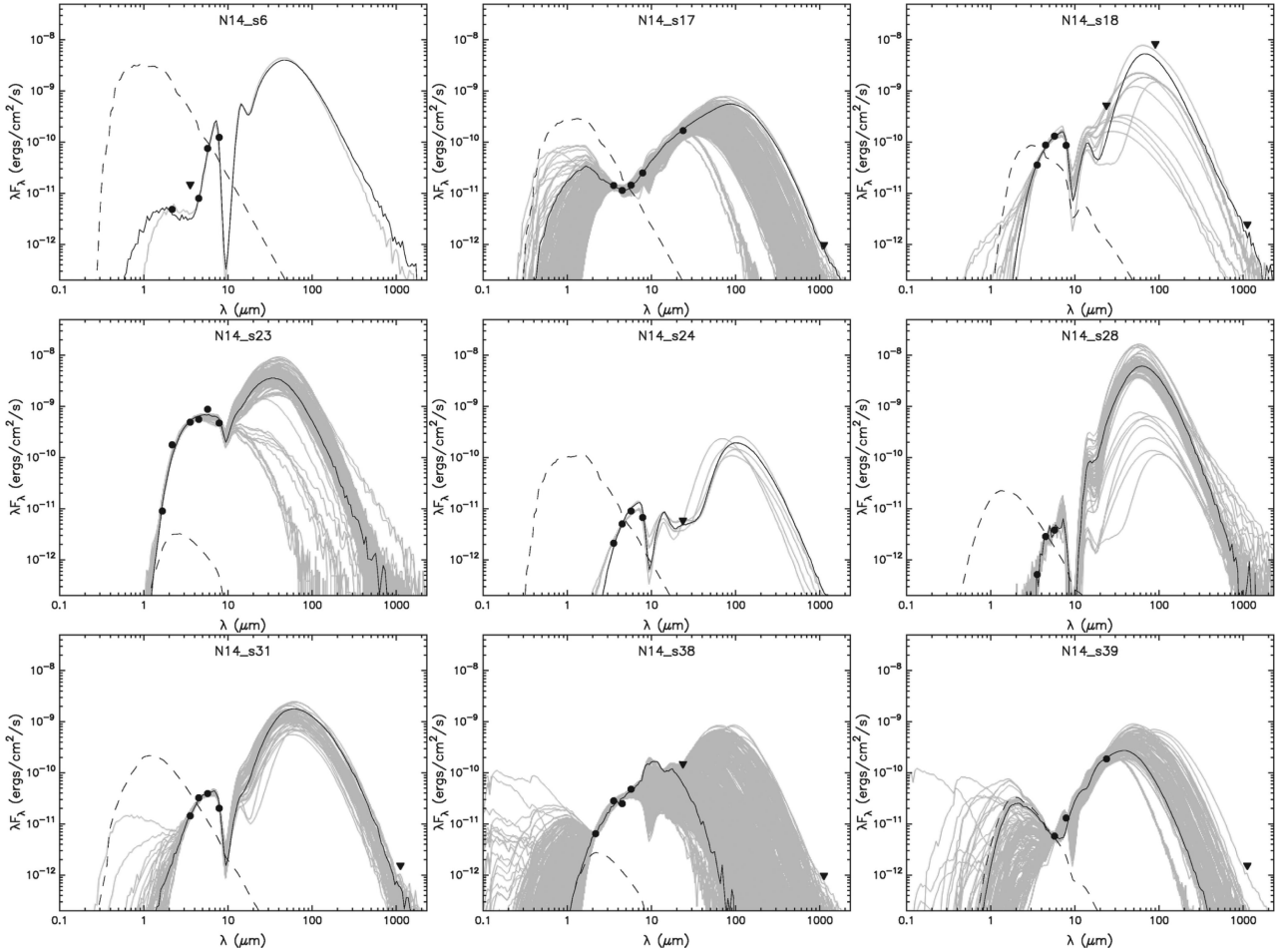


Figure 8. The SED plots of 9 out of 39 selected YSOs associated with the molecular and dust clumps are shown. The filled circles are observed fluxes of good quality (with filled triangles as upper limits) taken from the archives or published literature (see the text for more details) and the curves show the fitted model with the criterion $\chi^2 - \chi_{\text{best}}^2 < 3$. The thin black curve corresponds to the best-fitting model. The dashed curves represent photospheric contributions.

Table 2. NIR and *Spitzer* IRAC/GLIMPSE photometric magnitudes are listed for eight selected stars identified as probable ionizing candidate(s) inside the bubble N14. The estimated visual extinction A_V and absolute JHK_s magnitudes for each source is also tabulated.

ID	RA (2000)	Dec. (2000)	J (mag)	H (mag)	K_s (mag)	[3.6] (mag)	[4.5] (mag)	[5.8] (mag)	[8.0] (mag)	A_V (mag)	M_J	M_H	M_{K_s}	O-type star
1	18:16:18.79	-16:50:55.2	14.78	13.30	12.68	12.01	11.72	10.12	–	13.14	-1.67	-1.73	-1.53	–
2	18:16:22.14	-16:50:19.8	13.24	12.02	11.45	11.03	10.89	10.45	–	11.52	-2.75	-2.73	-2.58	–
3	18:16:22.50	-16:51:05.5	13.07	11.84	11.32	10.77	10.43	9.68	7.39	11.15	-2.82	-2.84	-2.67	–
4	18:16:19.98	-16:50:57.3	12.64	10.90	10.09	9.47	9.32	9.39	–	15.89	-4.59	-4.62	-4.44	O5V–O4V
5	18:16:16.86	-16:50:34.2	15.95	11.59	9.45	7.95	7.84	7.40	7.61	38.69	-7.76	-7.94	-7.67	–
6	18:16:21.36	-16:51:04.2	12.05	10.90	10.33	9.84	9.71	9.62	8.21	11.19	-3.85	-3.79	-3.66	O8V–O7.5V
7	18:16:22.15	-16:50:02.1	9.31	7.77	7.08	6.83	6.71	6.51	6.54	13.98	-7.38	-7.41	-7.23	–
8	18:16:21.50	-16:51:44.9	15.35	14.33	13.80	11.68	11.20	9.57	–	10.27	-0.29	-0.20	-0.09	–

and 7700 cm^{-3} for different turbulent velocity (a_s) values of 0.2, 0.4, 0.5 and 0.6 km s^{-1} , respectively. We have also estimated the kinematical time-scale of the molecular bubble of about 1.57 Myr ($\sim 4.5 \text{ pc}/2.8 \text{ km s}^{-1}$), assuming the bubble size of about 4.5 pc and velocity dispersion $\sim 2.8 \text{ km s}^{-1}$ from the $^{12}\text{CO}(J=3-2)$ map (see Beaumont & Williams 2010). The comparison of the dynamical age of the H II region with the kinematical time-scale of the expanding bubble and the fragmentation time-scale does not support the fragmentation of the molecular materials into clumps due to the ‘collect and collapse’ process around the bubble. Also, the average age of Class 0/I sources is reported to be about 0.10–0.44 Myr (see Evans et al. 2009), which is less than the fragmentation time-scale of the

molecular materials into clumps. Therefore, we suggest the possibility of triggered star formation by compression of the pre-existing dense clumps by the shock wave and/or small-scale Jeans gravitational instabilities in the collected materials. The YSO surface density contours clearly trace a clustering of Class I YSOs (s27–28, s30–33 and s39), with three intermediate masses (s30, s33 and s39) and two massive embedded sources (s28 and s31) associated with the dense dust clump at the eastern border of the bubble N14 (see Fig. 7 a and Table 1). We have also found that the s18 and s38 sources are also associated with the peak of different dust clumps around the bubble and the source ‘s18’ is identified as a new young massive protostar.

4 CONCLUSIONS

We have explored the triggered star formation scenario around the bubble N14 and its associated H II region using multi-wavelength observations. We find that there is clear evidence of collected material (molecular and cold dust) along the bubble around the N14 region. The surface density of YSOs reveals ongoing star formation and clustering of YSOs associated with the borders of the bubble. We conclude that the YSOs are being formed at the border of the bubble possibly by the expansion of the H II region. We further investigated the ‘collect-and-collapse’ process for triggered star formation around N14 using the analytical model of Whitworth et al. (1994). We have found that the dynamical age (~ 0.74 Myr) of the H II region is smaller, and the kinematical time-scale of the bubble (~ 1.57 Myr) is comparable to the fragmentation time-scale (~ 1.27 – 2.56 Myr) of accumulated gas layers in the region for 2071.5 cm^{-3} ambient density. The comparison of the dynamical age with the kinematical time-scale of the expanding bubble and the fragmentation time-scale does not support the fragmentation of the molecular materials into clumps due to the ‘collect and collapse’ process around N14, but suggests the possibility of triggered star formation by compression of the pre-existing dense clumps by the shock wave and/or small-scale Jeans gravitational instabilities in the collected materials. The YSO surface density contours clearly trace a clustering of Class I YSOs (~ 7 Class I sources with ~ 20 YSOs pc^{-2}) associated with the dense dust clump at the eastern border of the bubble N14. Also 5 young massive embedded protostars (about 8– $10 M_{\odot}$) and 15 intermediate mass (about 3– $7 M_{\odot}$) Class I YSOs are associated with the dust and molecular fragmented clumps at the borders of the bubble. It seems that the expansion of the H II region is also leading to the formation of these intermediate and massive Class I YSOs around the bubble N14.

ACKNOWLEDGMENTS

We thank the anonymous referee for a critical reading of the paper and several useful comments and suggestions, which greatly improved the scientific content of the paper. This work is based on data obtained as part of the UKIRT Infrared Deep Sky Survey and UWISH2 survey. This publication made use of data products from the Two Micron All Sky Survey (a joint project of the University of Massachusetts and the Infrared Processing and Analysis Center/California Institute of Technology, funded by NASA and NSF), archival data obtained with the *Spitzer* Space Telescope (operated by the Jet Propulsion Laboratory, California Institute of Technology under a contract with NASA). We thank Dirk Froebrich for providing the narrow-band H₂ image through the UWISH2 survey. We acknowledge support from a Marie Curie IRSES grant (230843) under the auspices of which some part of this work was carried out.

REFERENCES

Aguirre J. E. et al., 2011, *ApJS*, 192, 4
 Beaumont C. N., Williams J. P., 2010, *ApJ*, 709, 791
 Benjamin R. A. et al., 2003, *PASP*, 115, 935
 Bertoldi F., 1989, *ApJ*, 346, 735
 Brand J., Massi F., Zavagno A., Deharveng L., Lefloch B., 2011, *A&A*, 527, 62
 Carey S. J. et al., 2005, *BAAS*, 37, 1252
 Casali M. et al., 2007, *A&A*, 467, 777
 Churchwell E. et al., 2006, *ApJ*, 649, 759
 Churchwell E. et al., 2007, *ApJ*, 670, 428
 Churchwell E. et al., 2009, *PASP*, 121, 213
 Codella C., Felli M., Natale V., Palagi F., Palla F., 1994, *A&A*, 291, 261
 Deharveng L., Lefloch B., Zavagno A., Caplan J., Whitworth A.-P., Nadeau D., Martín S., 2003, *A&A*, 408, L25

Deharveng L., Lefloch B., Kurtz S., Nadeau D., Pomarès M., Caplan J., Zavagno A., 2008, *A&A*, 482, 585
 Deharveng L., Zavagno A., Schuller F., Caplan J., Pomarès M., De Breuck C., 2009, *A&A*, 496, 177
 Deharveng L. et al., 2010, *A&A*, 523, 6
 Dewangan L. K., Anandarao B. G., 2011, *MNRAS*, 414, 1526
 Dewangan L. K., Ojha D. K., Anandarao B. G., Ghosh S. K., Chakraborti S., 2012, *ApJ*, 756, 151
 Dye S. et al., 2006, *MNRAS*, 372, 1227
 Dyson J. E., Williams D. A., 1980, *Physics of the Interstellar Medium*. Halsted Press, New York, p. 204
 Elmegreen B. G., 2010, *EAS Publ. Ser.*, 51, 45
 Elmegreen B. G., Lada C. J., 1977, *ApJ*, 214, 725
 Evans N. J. et al., 2009, *ApJS*, 181, 321
 Fazio G. G. et al., 2004, *ApJS*, 154, 10
 Flaherty K. M., Pipher J. L., Megeath S. T., Winston E. M., Gutermuth R. A., Muzerolle J., Allen L. E., Fazio G. G., 2007, *ApJ*, 663, 1069
 Froebrich D. et al., 2011, *MNRAS*, 413, 480
 Getman K. V., Feigelson E. D., Garmire G., Broos P., Wang J., 2007, *ApJ*, 654, 316
 Gutermuth R. A., Megeath S. T., Myers P. C., Allen L. E., Pipher J. L., Fazio G. G., 2009, *ApJS*, 184, 18
 Hartmann L., Megeath S.-T., Allen L., Luhman K., Calvet N., D’Alessio P., Franco-Hernandez R., Fazio G., 2005, *ApJ*, 629, 881
 Helfand D. J., Becker R. H., White R. L., Fallon A., Tuttle S., 2006, *AJ*, 131, 2525
 Hodgkin S. T., Irwin M. J., Hewett P. C., Warren S. J., 2009, *MNRAS*, 394, 675
 Indebetouw R. et al., 2005, *ApJ*, 619, 931
 Ji W.-G., Zhou J.-J., Esimbek J., Wu Y.-F., Wu G., Tang X.-D., 2012, *A&A*, 544, 39
 Kryukova E., Megeath S.-T., Gutermuth R.-A., Pipher J., Allen T.-S., Allen L.-E., Myers P.-C., Muzerolle J., 2012, *ApJ*, 144, 31
 Kumar D. L., Anandarao B. G., 2010, *MNRAS*, 407, 1170
 Kwan J., 1997, *ApJ*, 489, 284
 Lawrence A. et al., 2007, *MNRAS*, 379, 1599
 Lefloch B., Lazareff B., 1994, *A&A*, 289, 559
 Lockman F. J., 1989, *ApJS*, 71, 469
 Martins F., Plez B., 2006, *A&A*, 457, 637
 Pomarès M. et al., 2009, *A&A*, 494, 987
 Povich M. S. et al., 2007, *ApJ*, 660, 346
 Reach W. T. et al., 2005, *PASP*, 117, 978
 Reach W. T. et al., 2006, *AJ*, 131, 1479
 Rieke G. H. et al., 2004, *ApJS*, 154, 25
 Robitaille T. P., Whitney B. A., Indebetouw R., Wood K., Denzmore P., 2006, *ApJS*, 167, 256
 Robitaille T. P., Whitney B. A., Indebetouw R., Wood K., 2007, *ApJS*, 169, 328
 Robitaille T. P. et al., 2008, *AJ*, 136, 2413
 Sevenster M. N., 2002, *ApJ*, 123, 2772
 Shetty R., Glover S. C., Dullemond C. P., Klessen R. S., 2011, *MNRAS*, 412, 1686
 Skrutskie M. F. et al., 2006, *AJ*, 131, 1163
 Smith M. D., Rosen A., 2005, *MNRAS*, 357, 1370
 Stetson P. B., 1987, *PASP*, 99, 191
 Varricatt W. P., 2011, *A&A*, 527, 97
 Watson C. et al., 2008, *ApJ*, 681, 1341
 Whitney B. A. et al., 2008, *AJ*, 136, 18
 Whitworth A. P., Bhattal A. S., Chapman S. J., Disney M. J., Turner J. A., 1994, *MNRAS*, 268, 291
 Wood D. O. S., Churchwell E., 1989, *ApJS*, 69, 831
 Zavagno A., Deharveng L., Comerón F., Brand J., Massi F., Caplan J., Russeil D., 2006, *A&A*, 446, 171
 Zavagno A. et al., 2010, *A&A*, 518, L81
 Zinnecker H., Yorke H. W., 2007, *ARA&A*, 45, 481